

# Journal of Mechanics of Materials and Structures

**TUNING STRESS CONCENTRATIONS THROUGH  
EMBEDDED FUNCTIONALLY GRADED SHELLS**

Xiaobao Li, Yiwei Hua, Chenyi Zheng and Changwen Mi

**Volume 13, No. 3**

**May 2018**





## TUNING STRESS CONCENTRATIONS THROUGH EMBEDDED FUNCTIONALLY GRADED SHELLS

XIAOBAO LI, YIWEI HUA, CHENYI ZHENG AND CHANGWEN MI

In this work, we explore the possibility of tuning stress concentrations in materials by judiciously designing embedded functionally graded shells. Specifically, we choose thick-walled cylinders to illustrate our central idea. We specifically consider the boundary value problem of a radially varying graded shell bonded to a thick-walled cylinder. We obtain closed-form solutions and our parametric numerical studies suggest that a graded soft shell can effectively drive the stress concentration from the inner surface of the shell to the shell-cylinder interface. For any boundary loading, an optimal inhomogeneity index that balances the stress concentrations along the inner surface and the interface can be identified. Using the solution to a completely homogeneous cylinder as a benchmark, the stress concentration factor can be reduced by more than 40%. The results of this work suggest the significant potential of functionally graded materials for tailoring the stress concentrations of engineering structures by bonding a properly designed inhomogeneous layer to the perimeter of geometric defects.

### 1. Introduction

Stresses may be significantly amplified around regions with geometric discontinuities and abrupt changes in material properties or load intensities. This phenomenon is known as stress concentrations. It is often responsible for structural failure, e.g., damage and fracture, and is generally measured by the use of stress concentration factors (SCFs). Consequently, reducing the stress concentration factor of engineering elements and structures is of significant interest and importance in practice. In other words, optimization of stress distribution is desired for those structures with stress concentrations, in particular, for plates and cylinders containing holes. Since the 1960s, many studies have been continuously devoted to the stress analysis of plates with holes of various shapes under different loading conditions [Savin 1961; Theocaris and Petrou 1986; Ukadgaonker and Rao 1999; Rezaeepazhand and Jafari 2010]. More recently, Wu and Mu [2003] developed a computational method to estimate the SCFs of isotropic and orthotropic plates as well as cylinders with a circular cutout. Later, Yang et al. [2008; 2010b] investigated the stress and strain concentrations of a plate containing a circular hole. By the use of the complex variable method, Batista [2011] calculated the stress concentration around a hole with complex geometry in an infinite elastic plate. Patel and Sharma [2017] proposed a numerical approach to study the stress field around polygonal cutouts with complex geometries in an orthotropic media. On the basis of these literature studies, Nagpal et al. [2012] presented a complete analysis and overview on techniques focusing on the relief of stress concentrations in materials and structures with cavities.

---

*Keywords:* functionally graded material, stress concentration, method of stress function, thick-walled cylinder, elasticity theory.

The above studies all focused on homogeneous materials with geometric defects. Functionally graded material (FGM) is a class of composite materials that possess continuous variation of material properties along certain spatial dimensions. This distinguishing feature eliminates the sharp discontinuity in material properties that naturally arise when bridging materials with drastically different properties. FGMs may thus help regulate the stress distribution and function performance of composite structures. Due to this, FGMs have received considerable attention in the past two decades and found a number of applications in aerospace engineering [Marin 2005] and biomedical engineering [Watari et al. 2004], among others [Kawasaki and Watanabe 2002; Müller et al. 2003; Chen et al. 2012].

Up to the present, numerous studies have reported applications of FGMs in engineering structures, and in particular, their effect on stress reduction in structures with geometric defects [Jin and Batra 1996; Chi and Chung 2006a; 2006b; Birman and Byrd 2007; Yang et al. 2015]. Kubair and Bhanu-Chandar [2008] solved the SCFs due to a circular hole in a functionally graded panel and found that the stress concentrations can be reduced when the Young's modulus is allowed to progressively increase away from the center of the hole. Yang et al. [2010a] also analyzed the stress distribution of a functionally graded plate with a circular hole and reported significant stress relief as the Young's modulus is allowed to radially increase. Later, Mohammadi et al. [2011] revisited the stress concentration problem around a circular hole in an infinite FGM plate subjected to different loading conditions. More recently, Yang et al. [2015] further studied the three-dimensional equilibrium problem of a voided transversely isotropic FGM plate subjected to loading applied on the remote boundary of the plate. Several other studies on the stress concentration analysis of FGM plates under different conditions include [Kubair 2013; Sburlati et al. 2014; Gouasmi et al. 2015; Mohammadi et al. 2016]. Jha et al. [2013] supplied a comprehensive review on various theories of FGM plates and their applications.

In addition to plates, stress concentrations in another important engineering structure, i.e., graded cylinders, under various loading conditions have also been studied [Pan and Roy 2006; Chen and Lin 2010; Batra and Nie 2010; Nie and Batra 2010; Nie et al. 2011; Sadeghi et al. 2012; Ghannad et al. 2013; Chen 2015]. Horgan and Chan [1999] solved the stress field in a pressure vessel with radially graded Young's modulus. By comparing with a completely homogeneous vessel, they showed the significant difference in stress distribution. Tutuncu [2007] further investigated the stress distribution in cylindrical vessels with exponentially varying modulus along radial axis. Oral and Anlas [2005] derived a closed-form stress solution for an orthotropic cylindrical pressure vessel with inhomogeneous material properties. By treating either the elastic stiffness or Poisson's ratio as a constant, but not both, Dryden and Batra [2013] studied the axisymmetric plane strain problem of a graded cylinder under hydrostatic loading. They also successfully designed an equivalent homogeneous vessel with the same stress concentration level as that of a graded one. Xin et al. [2014] further considered the possible effects of Poisson's ratio on stresses and displacements and presented a theoretical formulation for graded thick-walled cylinders.

Although many studies have been devoted to reducing stress concentrations in pressure vessels, most of them focus on geometric defects embedded in infinite domains under hydrostatic boundary loads. Nonetheless, it has been shown that graded materials work best as a coating or a transitional layer bridging two components with drastically different material properties. When employed this way, an FGM component is able to significantly improve the mechanical behavior of the original structure, including the conventionally undesired stress concentrations [Kashtalyan and Menshykova 2007; Sburlati 2012; Sburlati et al. 2013; Chu et al. 2015].

By the use of a thin FGM ring, Sburlati [2013] explored the possibility to relieve the stress concentration around the circular hole in a homogeneous plate under far-field uniaxial tension. They demonstrated that the SCF around the hole perimeter can be significantly reduced by a proper choice of the grading parameter of the annular ring. Shortly thereafter, they extended their model to take into account both a perfect bonding and a pure sliding condition at the ring/plate interface [Sburlati et al. 2014]. Analytical solutions due to four types of simple far-field loads are presented. Yang and Gao [2016] also confirmed that by using a properly graded thin shell around an elliptic hole in an infinite plate, the SCFs may be effectively reduced.

Motivated by these studies, the primary goal of the present study is to propose a solution to mitigating stress concentrations in a thick-walled cylinder subjected to an arbitrary boundary load. We believe that it is a promising way to improve the stress distribution in thick-walled cylinders by introducing an inhomogeneous annular shell, treated as a thin coating perfectly bonded to the inner surface of a circular cylinder. The Young's modulus of the inhomogeneous shell is allowed to vary along its radial dimension by following a power-law function, whereas the Poisson's ratio of the shell is kept as a constant without any gradation. The problem is formulated with the method of Airy stress function. For the case of inhomogeneous material properties, the conventional biharmonic equation that must be satisfied by the stress function of a homogeneous medium becomes a general fourth-order differential equation of Euler-type. Successful tackling of this differential equation renders us an analytical solution to the stresses and displacements of the proposed problem.

The remainder of this paper is organized as follows. Section 2 presents the Airy stress function formulation of the proposed problem and its analytical solutions due to both an all-around traction and an arbitrary biaxial load. In Section 3, extensive parametric studies are performed to illustrate the effects of the inhomogeneity index of the embedded shell and the traction ratio along perpendicular directions on the stress distribution and stress concentrations. Whenever possible, the benchmark solution to a completely homogeneous cylinder is computed and used as a comparison basis. Finally, in Section 4, a few concluding remarks that were informed from both the analytical solutions and numerical studies are drawn.

## 2. Formulation and method of solution

As shown in Figure 1, the problem under consideration is composed of a thick-walled cylinder reinforced by a perfectly bonded thin shell, both of finite thickness. The Young's modulus of the cylinder is assumed to be homogeneous while that of the inner shell is treated as a radially graded quantity, i.e.,

$$E^{(i)} = E^{(o)} \left( \frac{r}{r_0} \right)^m, \quad (1)$$

where  $m$  represents the inhomogeneity index of the grade shell and therefore should be a real number. The superscripts  $(i)$  and  $(o)$  are used to denote the quantities that belong to the inner shell and the outer cylinder, respectively. The inhomogeneity index serves as a governing parameter for tuning the relative stiffness between the shell and the cylinder. The power law function (1) was specialized so that the material properties at the shell-cylinder interface ( $r = r_0$ ) remain continuous. Since the effect of Poisson's ratio ( $\nu$ ) has proven to be very marginal when compared to that of the elastic modulus, see for example [Sburlati et al. 2014, Table 3], it seems reasonable to fix it as an equal constant in both domains. The combination deforms under the application of a uniform boundary loading:  $\sigma_x = p$  and  $\sigma_y = q$  at the

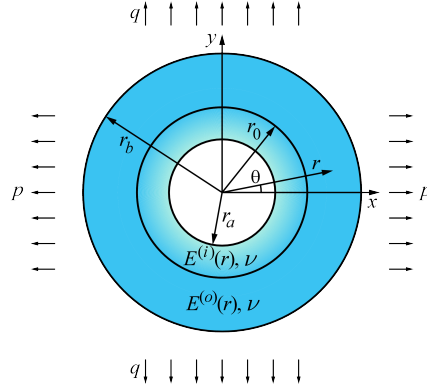


**Figure 1.** Geometry and loading configuration of the problem.

outer boundary of the cylinder. Such a loading condition is general in the sense that an arbitrary uniform boundary traction can always be converted into this form, with a proper rotation of coordinates.

Due to the axial symmetry of the structure, polar coordinates become a natural choice to formulate and solve the problem. In the absence of body forces, the two-dimensional equations of equilibrium are thus given by

$$\frac{\partial \sigma_r}{\partial r} + \frac{1}{r} \frac{\partial \sigma_{r\theta}}{\partial \theta} + \frac{\sigma_r - \sigma_\theta}{r} = 0, \quad \frac{\partial \sigma_{r\theta}}{\partial r} + \frac{1}{r} \frac{\partial \sigma_\theta}{\partial \theta} + \frac{2}{r} \sigma_{r\theta} = 0, \quad (2)$$

where  $\sigma_r$ ,  $\sigma_\theta$ , and  $\sigma_{r\theta}$  are the normal and shear stress components, respectively. The strain-displacement relations read

$$\varepsilon_r = \frac{\partial u_r}{\partial r}, \quad \varepsilon_\theta = \frac{1}{r} \left( u_r + \frac{\partial u_\theta}{\partial \theta} \right), \quad \varepsilon_{r\theta} = \frac{1}{2} \left( \frac{1}{r} \frac{\partial u_r}{\partial \theta} - \frac{u_\theta}{r} + \frac{\partial u_\theta}{\partial r} \right). \quad (3)$$

The present problem is more reasonable to be modeled as a plane strain one. Nonetheless, it is well known that plane strain formulation generally results in more complicated mathematical expressions when compared to those of plane stress formulation. For simplicity, we have chosen to first formulate the present problem in terms of the plane stress constitutive law:

$$\varepsilon_r = \frac{1}{E(r)} (\sigma_r - \nu \sigma_\theta), \quad \varepsilon_\theta = \frac{1}{E(r)} (\sigma_\theta - \nu \sigma_r), \quad \varepsilon_{r\theta} = \frac{2(1+\nu)}{E(r)} \sigma_{r\theta}. \quad (4)$$

Later in the numerical analysis and discussion (Section 3), the plane strain version of these equations are obtained by the change of material properties:  $E \rightarrow E/(1-\nu^2)$  and  $\nu \rightarrow \nu/(1-\nu)$ .

For problems formulated in terms of stresses, it is well known that in addition to the above equations, the strain compatibility condition must also be satisfied:

$$\frac{\partial^2 \varepsilon_\theta}{\partial r^2} + \frac{1}{r^2} \frac{\partial^2 \varepsilon_r}{\partial \theta^2} + \frac{2}{r} \frac{\partial \varepsilon_\theta}{\partial r} - \frac{1}{r} \frac{\partial \varepsilon_r}{\partial \theta} = \frac{1}{r} \frac{\partial^2 \varepsilon_{r\theta}}{\partial r \partial \theta} + \frac{1}{r^2} \frac{\partial \varepsilon_{r\theta}}{\partial \theta}. \quad (5)$$

Since the present problem is formulated within the framework of the linearized theory of elasticity, the biaxial boundary tractions shown in Figure 1 can safely be superposed from the two uniaxial tractions along individual coordinate axes. As a result, it would be sufficient to develop a solution due to the traction load  $\sigma_x = p$ . The solution due to  $\sigma_y = q$  can readily be obtained by making the replacements  $p \rightarrow q$  and  $\theta \rightarrow \theta + \frac{1}{2}\pi$ .

With the help of the transformation matrix between the regular Cartesian and polar coordinates, it is easy to find the polar components for the uniaxial traction  $\sigma_x = p$ :

$$\sigma_r = \frac{1}{2}p(1 + \cos 2\theta), \quad \sigma_{r\theta} = -\frac{1}{2}p \sin 2\theta. \quad (6)$$

The boundary conditions (6) can further be decomposed into an axial symmetric component,

$$\sigma_r = \frac{1}{2}p, \quad (7a)$$

$$\sigma_{r\theta} = 0, \quad (7b)$$

and an antisymmetric component,

$$\sigma_r = \frac{1}{2}p \cos 2\theta, \quad \sigma_{r\theta} = -\frac{1}{2}p \sin 2\theta. \quad (8)$$

Irrespective of the traction conditions applied at the outer boundary of the cylinder, the inner surface of the embedded shell is always free of tractions:

$$\sigma_r(r_a, \theta) = 0, \quad (9a)$$

$$\sigma_{r\theta}(r_a, \theta) = 0. \quad (9b)$$

The perfect bonding condition between the two material components requires that both the displacements and the stress tractions must be continuous across the shell-cylinder interface:

$$[\sigma_r(r_0, \theta)] = 0, \quad (10a)$$

$$[\sigma_{r\theta}(r_0, \theta)] = 0, \quad (10b)$$

$$[u_r(r_0, \theta)] = 0, \quad (10c)$$

$$[u_\theta(r_0, \theta)] = 0, \quad (10d)$$

where the square brackets denote the jumps of displacements and stress tractions.

To solve the problem we use the Airy stress function in the general form  $\varphi = \varphi(r, \theta)$ , with the polar stress components written as

$$\sigma_r = \frac{1}{r} \frac{\partial \varphi(r, \theta)}{\partial r} + \frac{1}{r^2} \frac{\partial^2 \varphi(r, \theta)}{\partial \theta^2}, \quad \sigma_\theta = \frac{\partial^2 \varphi(r, \theta)}{\partial r^2}, \quad \sigma_{r\theta} = \frac{1}{r^2} \frac{\partial \varphi(r, \theta)}{\partial \theta} - \frac{1}{r} \frac{\partial^2 \varphi(r, \theta)}{\partial r \partial \theta}. \quad (11)$$

In the remainder of this section, we aim to develop analytical solutions to both the symmetric (7) and the antisymmetric (8) boundary conditions.

**2.1. Axial symmetric solution.** When the structure shown in Figure 1 is subjected to an all-around traction of magnitude  $\frac{1}{2}p$ , i.e., (7), the Airy stress function becomes azimuthally independent:  $\varphi = \varphi_0(r)$ . For this case, the compatibility condition can be reformulated in terms of the Airy stress function by combining equations (11), (4), and (5):

$$\frac{d^4 \varphi_0(r)}{dr^4} + \frac{2(1-m)}{r} \frac{d^3 \varphi_0(r)}{dr^3} + \frac{(m^2 + \nu m - m - 1)}{r^2} \frac{d^2 \varphi_0(r)}{dr^2} - \frac{(m+1)(\nu - 1)}{r^3} \frac{d \varphi_0(r)}{dr} = 0. \quad (12)$$

This equation is an ordinary differential equation of Euler type whose solution is

$$\varphi_0^{(o)}(r) = z_1 \ln(r) + z_2 r^2 \quad (13)$$

for the outer cylinder and

$$\varphi_0^{(i)}(r) = C_1 r^{m/2+\rho/2+1} + C_2 r^{m/2-\rho/2+1} \quad (14)$$

for the inner shell, where  $z_1, z_2, C_1, C_2$  represent unknown coefficients to be determined by imposing the boundary conditions and  $\rho = \sqrt{m^2 + 4 - 4\nu m}$ . It is easy to show for the practical range of Poisson's ratio, e.g.,  $0 < \nu < 0.5$ , the parameter  $\rho$  is always a real number. Substituting (13) and (14) back into (11) yields

$$\sigma_r^{(o)} = 2z_2 + \frac{z_1}{r^2}, \quad \sigma_\theta^{(o)} = 2z_2 - \frac{z_1}{r^2}, \quad (15a)$$

$$\sigma_r^{(i)} = \frac{(m + \rho + 2)r^{m/2+\rho/2}C_1 + (m - \rho + 2)r^{m/2-\rho/2}C_2}{2r}, \quad (15b)$$

$$\sigma_\theta^{(i)} = \frac{(m + \rho)(m + \rho + 2)r^{m/2+\rho/2}C_1 + (m - \rho)(m - \rho + 2)r^{m/2-\rho/2}C_2}{2r}. \quad (15c)$$

The four unknown coefficients ( $z_1, z_2, C_1, C_2$ ) are determined by the boundary conditions (7a), (9a), (10a), and (10c)

$$\begin{aligned} z_1 &= -\frac{mr_b^2 r_0^2 p}{2\Omega} (r_a^\rho (m - 2\nu - \rho)(2 + m + \rho) - r_0^\rho (m - 2\nu + \rho)(2 + m - \rho)), \\ z_2 &= \frac{r_b^2 r_a^\rho p}{4\Omega} (2 + m + \rho)(m^2 + m(2 - 2\nu - \rho) + 2(2 - \rho)) \\ &\quad - \frac{r_b^2 r_0^\rho p}{4\Omega} (2 + m - \rho)(m^2 + m(2 - 2\nu + \rho) + 2(2 + \rho)), \\ C_1 &= -\frac{2r_b^2 r_0^{1-m/2+\rho/2} (2 + m - \rho)p}{\Omega}, \quad C_2 = -\frac{2r_b^2 r_a^\rho r_0^{1-m/2+\rho/2} (2 + m + \rho)p}{\Omega}, \end{aligned} \quad (16)$$

where

$$\begin{aligned} \Omega &= r_a^\rho (2 + m + \rho)(mr_0^2(\rho - m + 2\nu) + r_b^2(m^2 + m(2 - 2\nu - \rho) + 2(2 - \rho))) \\ &\quad + r_0^\rho (2 + m - \rho)(mr_0^2(\rho + m - 2\nu) - r_b^2(m^2 + m(2 - 2\nu + \rho) + 2(2 + \rho))). \end{aligned} \quad (17)$$

**2.2. Antisymmetric solution.** Given the antisymmetric boundary conditions (8), the Airy stress function for both domains must assume the form  $\varphi = \varphi_2(r) \cos 2\theta$ . In view of (11) and (4), the strain compatibility (5) can now be recast in terms of the function  $\varphi_2(r)$ . For the outer cylinder and the inner shell, the compatibility condition becomes

$$\left( \frac{d^2}{dr^2} + \frac{1}{r} \frac{d}{dr} - \frac{4}{r^2} \right) \left( \frac{d^2}{dr^2} + \frac{1}{r} \frac{d}{dr} - \frac{4}{r^2} \right) \varphi_2^{(o)}(r) = 0 \quad (18)$$

and

$$\begin{aligned} \frac{d^4 \varphi_2^{(i)}(r)}{dr^4} + \frac{2(1-m)}{r} \frac{d^3 \varphi_2^{(i)}(r)}{dr^3} + \frac{(m^2 + \nu m - m - 9)}{r^2} \frac{d^2 \varphi_2^{(i)}(r)}{dr^2} \\ - \frac{(m+1)(m\nu - 9)}{r^3} \frac{d \varphi_2^{(i)}(r)}{dr} + \frac{4m(m\nu + \nu m - 3)}{r^4} \varphi_2^{(i)}(r) = 0, \end{aligned} \quad (19)$$



respectively. Benefitting from the constant material properties in the cylinder, (18) is easy to solve and the corresponding stress function is found to be

$$\varphi_2^{(o)}(r, \theta) = \left( z_{24} + \frac{z_{23}}{r^2} + z_{21}r^2 + z_{22}r^4 \right) \cos 2\theta. \quad (20)$$

Although the differential equation (19) is much more complicated, it is a fourth-order Euler equation, whose solution can be put in the form

$$\varphi_2^{(i)}(r, \theta) = r^{m+1} (D_1 A_1(r) + D_2 A_2(r) + D_3 B_1(r) + D_4 B_2(r)) \cos 2\theta. \quad (21)$$

The eight coefficients ( $D_1, D_2, D_3, D_4, z_{21}, z_{22}, z_{23}, z_{24}$ ) are all unknown constants to be evaluated from the boundary conditions (8), (9), and (10). The four functions ( $A_1, A_2, B_1, B_2$ ) depend solely on the radial coordinate:

$$A_1(r) = r^{-m/2-\alpha/2}, \quad A_2(r) = r^{-m/2+\alpha/2}, \quad B_1(r) = r^{-m/2-\beta/2}, \quad B_2(r) = r^{-m/2+\beta/2}, \quad (22)$$

where

$$\alpha = \sqrt{m^2 + 2m - 2\nu m + 20 - 2\sqrt{m^2 + \nu^2 m^2 - 14\nu m^2 - 32\nu m + 32m + 64}}, \quad (23a)$$

$$\beta = \sqrt{m^2 + 2m - 2\nu m + 20 + 2\sqrt{m^2 + \nu^2 m^2 - 14\nu m^2 - 32\nu m + 32m + 64}}. \quad (23b)$$

For real  $\alpha$  and  $\beta$ , the inhomogeneity index  $m$  has to fall in the interval  $[0, 8(2 - \sqrt{3})/(\nu + 4\sqrt{3} - 7)]$ . Given the Airy stress functions (20) and (21), it is straightforward to find the stress components from (11):

$$\sigma_r^{(o)} = -2 \left( z_{21} + \frac{2z_{24}}{r^2} + \frac{3z_{23}}{r^4} \right) \cos 2\theta, \quad (24a)$$

$$\sigma_\theta^{(o)} = 2 \left( z_{21} + 6z_{22}r^2 + \frac{3z_{23}}{r^4} \right) \cos 2\theta, \quad (24b)$$

$$\sigma_{r\theta}^{(o)} = 2 \left( z_{21} + 3z_{22}r^2 - \frac{z_{24}}{r^2} - \frac{3z_{23}}{r^4} \right) \sin 2\theta, \quad (24c)$$

$$\sigma_r^{(i)} = \frac{(m - \alpha - 6)A_1(r)D_1 + (m - \beta - 6)B_1(r)D_3}{2r^{1-m}} \cos 2\theta + \frac{(m + \alpha - 6)A_2(r)D_2 + (m + \beta - 6)B_2(r)D_4}{2r^{1-m}} \cos 2\theta, \quad (24d)$$

$$\sigma_\theta^{(i)} = \frac{(m - \alpha)(m - \alpha + 2)A_1(r)D_1 + (m - \beta)(m - \beta + 2)B_1(r)D_3}{4r^{1-m}} \cos 2\theta + \frac{(m + \alpha)(m + \alpha + 2)A_2(r)D_2 + (m + \beta)(m + \beta + 2)B_2(r)D_4}{4r^{1-m}} \cos 2\theta, \quad (24e)$$

$$\sigma_{r\theta}^{(i)} = \frac{(m - \alpha)A_1(r)D_1 + (m - \beta)B_1(r)D_3 + (m + \alpha)A_2(r)D_2 + (m + \beta)B_2(r)D_4}{r^{1-m}} \sin 2\theta. \quad (24f)$$

Simultaneously enforcing the boundary conditions at the inner surface of the shell (9), at the shell-cylinder interface (10), and at the outer boundary of the cylinder (8) solves the eight unknown coefficients

$$z_{21} = \frac{r_b^2 p \sum_{i=1}^4 \sum_{j>i} (\xi_i - \xi_j) \eta_{ij} a_i a_j}{4 \sum_{i=1}^4 \sum_{j>i} (\xi_i - \xi_j) \psi_{ij} a_i a_j}, \quad (25a)$$

$$z_{22} = \frac{p \sum_{i=1}^4 (2r_b^2 r_0^2 (4z_{21} + 1) \lambda_{i4} - 4z_{21} r_0^4 \lambda_{i1} - (4z_{21} + 1) r_b^4 \lambda_{i3}) a_i}{4 \sum_{i=1}^4 (r_0^6 \lambda_{i2} + 2r_b^6 \lambda_{i3} - 3r_b^4 r_0^2 \lambda_{i4}) a_i}, \quad (25b)$$

$$z_{23} = \frac{r_b^4 r_0^4 p \sum_{i=1}^4 \sum_{j>i} (\xi_i - \xi_j) \mu_{ij} a_i a_j}{4 \sum_{i=1}^4 \sum_{j>i} (\xi_i - \xi_j) \psi_{ij} a_i a_j}, \quad (25c)$$

$$z_{24} = \frac{r_b^2 p \sum_{i=1}^4 (12z_{21} r_b^2 r_0^4 \lambda_{i1} - 2(4z_{21} + 1) r_0^6 \lambda_{i2} + (4z_{21} + 1) r_b^6 \lambda_{i3}) a_i}{4 \sum_{i=1}^4 (r_0^6 \lambda_{i2} + 2r_b^6 \lambda_{i3} - 3r_b^4 r_0^2 \lambda_{i4}) a_i}, \quad (25d)$$

$$D_i = p \sum_{j=1}^4 \zeta_j z_{2j} \lambda_{ij}, \quad i, j = 1, 2, 3, 4, \quad (25e)$$

where  $\lambda_{ij}$ ,  $\eta_{ij}$ ,  $\mu_{ij}$ , and  $\psi_{ij}$  are elements of  $4 \times 4$  matrices while  $\xi_i$ ,  $a_i$ , and  $\zeta_i$  are those of vectors possessing four components. Although the solution procedure was straightforward, the mathematical expressions for these parameters are quite lengthy. For brevity, they are documented in the Appendix.

At this point, the complete solution to the uniaxial traction load  $\sigma_x = p$  applied at the outer boundary of the cylinder can readily be obtained by superposing the axial symmetric (15) and the antisymmetric (24a) stresses. For the case of  $\sigma_y = q$ , stresses can be adapted by making the replacements  $\theta \rightarrow \theta + \frac{1}{2}\pi$ ,  $\cos 2\theta \rightarrow -\cos 2\theta$ , and  $\sin 2\theta \rightarrow -\sin 2\theta$ , without affecting the axial symmetric part.

In summary, we solved the boundary value problem presented in Figure 1 by the method of Airy stress function. The solution algorithm follows closely to typical plane elasticity problems as explained in the classical theory of elasticity [Barber 2010]. First, the governing equations of plane elasticity (2)–(5) were combined to construct the compatibility condition on stress components. Second, by the introduction of Airy stress function (11), the condition was further transformed into a fourth-order differential equation whereas both equilibrium equations in (2) are found to be identically satisfied. Third, the compatibility equation in terms of Airy stress function was analytically solved for both axial symmetric and antisymmetric uniform boundary loading. For the two cases, the solutions contain four and eight integration constants, respectively. Finally, they were uniquely determined by implementing the traction boundary conditions at the inner and outer surfaces of the cylinder and the perfect bonding assumption at the graded shell-cylinder interface.

### 3. Numerical results and discussion

Although we have obtained the analytical solution to the present problem it is mathematically lengthy and therefore inconvenient to demonstrate the effect of the embedded FGM shell. The numerical studies that will be presented in this section are for two purposes. The first of which is to compare the differences in stress concentrations of a thick-walled cylinder, if any, due to an FGM inner shell and a completely homogeneous one. The other is to explore the mechanism of mitigating stress concentrations and thus to enhance the structural integrity of pressure vessels.

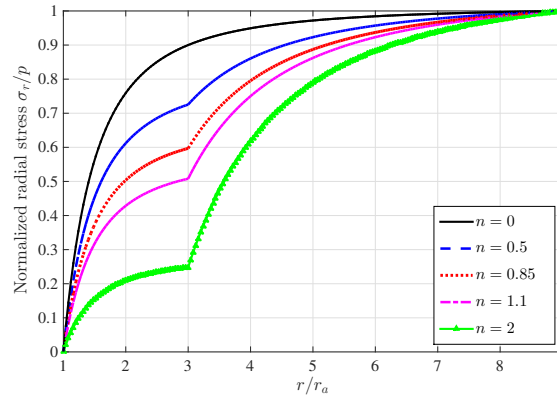


**Figure 2.** Variation of the normalized radial stress as a function of the radial coordinate for five homogeneous shells.

Calculations require specific values for material properties, geometric parameters, and mechanical loads. We assume that the Poisson's ratio of both the cylinder and the shell is  $\nu = 0.3$ , because of its very limited impact on stress concentrations [Sburlati 2013]. Due to the absence of the size-dependent effect, it is sufficient to assign just two radii ratios  $r_0/r_a = 3$  and  $r_b/r_a = 9$  for the geometric parameters. All stress values are normalized with respect to the applied boundary traction. In addition, for comparison purposes the case of a homogeneous inner shell that possesses the same material properties as those of the outer cylinder is also calculated whenever necessary. As aforementioned in Section 2, all analysis and discussion to be presented in this section were performed against the plane strain condition. In the remainder of this section, we first consider the case of a uniform all-around boundary loading, followed by the more general case of an arbitrary biaxial traction.

### 3.1. Axial symmetric traction loading.

**3.1.1. A homogeneous inner shell with different properties from those of the outer cylinder.** For comparison purposes, let us first consider a completely homogeneous inner shell but with a different Young's modulus than that of the outer cylinder

$$E^{(i)} = \left(\frac{r_a}{r_0}\right)^n E^{(o)}, \quad (26)$$

where  $n$  is an arbitrary constant representing the relative stiffness between the shell and the cylinder. For nonzero  $n$ , it is seen that there is a discontinuity in material properties across the shell-cylinder interface. This simplified case may be treated as a degeneracy of the solution developed for an FGM shell. The Airy stress function of the shell thus takes the same form as that of the cylinder (13). As a result, the stress fields in both domains share the same distribution pattern; see (15a) and (15b). The four constants of integration can subsequently be determined by imposing the boundary conditions at the material's surfaces ( $r_a, r_b$ ) and the shell-cylinder interface ( $r_0$ ). For the special case of a completely homogeneous cylinder, the stress field can be obtained by further setting the index  $n$  as zero.

Figure 2 shows the normalized radial stress distribution for different values of  $n$  ( $n = 0, 0.5, 0.85, 1.1, 2$ ). It is seen that for positive  $n$ , the radial stress is always smaller than that of a completely homogeneous

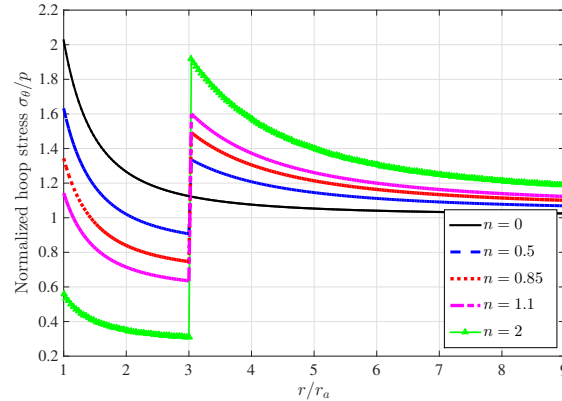


**Figure 3.** Variation of the normalized hoop stress as a function of the radial coordinate for five homogeneous shells.

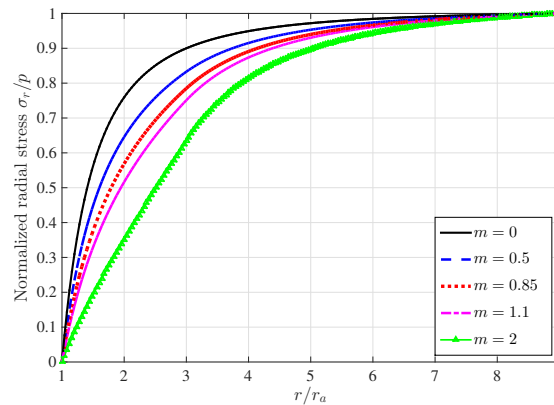
cylinder ( $n = 0$  or  $E^{(i)} = E^{(o)}$ ). In particular, the radial stress is significantly reduced at the shell-cylinder interface. Because in this case the Young's modulus of the embedded shell is smaller than that of the outer cylinder, the slope of the radial stress curve becomes smaller in the shell and larger in the cylinder, when compared to the case of  $n = 0$ . With increasing  $n$ , both the slope and general level of the radial stress in the shell decrease. For the outer cylinder, an opposite trend can be confirmed. It is also noticed that at the shell-cylinder interface the radial stress is not differentiable, although the stress value remains continuous. For all values of  $n$ , the maximum stress always appears on the outer surface of the cylinder and is equal to the applied all-around tension, indicating that stress concentrations are not of a concern for the radial stress component.

Figure 3 shows the variation of the normalized hoop stress for the same five cases that were studied in Figure 2. It is seen that for the case of a completely homogeneous cylinder ( $n = 0$ ), the stress concentration factor reads  $\sigma_\theta/p = 2.025$ . For  $n \neq 0$  the hoop stress experiences a sharp discontinuity across the shell-cylinder interface. The softer the inner shell is the larger the stress discontinuity becomes. Moreover, the stress level becomes lower in the embedded shell but higher in the outer cylinder. In both domains, the hoop stress component decays with the radial coordinate. Furthermore, it is interesting to note the trade-off pattern between the stress levels at the rim of the inner shell and at the shell-cylinder interface. With increasing  $n$ , the stress concentration factor at  $r = r_a$  monotonically decreases. The opposite is true for the stress concentration factor at the shell-cylinder interface. This behavior suggests an optimized value of the relative stiffness parameter ( $n = 0.725$ ,  $E^{(i)}/E^{(o)} \approx 0.451$ ) such that the stress concentration factors at the shell surface and at the shell-cylinder interface become an equal value ( $\sigma_\theta/p = 1.446$ ). The stress concentration level has reduced by 27.7% when compared with a completely homogeneous thick-walled cylinder.

**3.1.2. A graded thin shell perfectly bonded to a thick-walled cylinder.** In this subsection, we aim to analyze the stress distribution inside an FGM shell perfectly bonded to the inner surface of a thick-walled cylinder. The combination is still subjected to an axisymmetric all-around tension at the outer surface of the cylinder  $r = r_b$ . The Young's modulus of the FGM shell is allowed to vary along its radial dimension, by following the power-law function (1). To investigate the variation of stresses, the four constants of

$m$	$z_1/p$	$z_2/p$	$C_1/p$	$C_2/p$
0.5	-1.692	0.510	0.366	-2.417
0.85	-2.176	0.513	0.272	-1.216
1.1	-2.521	0.516	0.212	-0.819
2	-3.698	0.523	0.071	-0.233

**Table 1.** Numerical values of the four constants of integration in (16) that are used for plotting Figures 4 and 5, left. The other parameters are set as  $\nu = 0.3$ ,  $r_0/r_a = 3$ , and  $r_b/r_a = 9$ .



**Figure 4.** Variation of the normalized radial stress along the radial dimension for five inhomogeneous shells.

integration in (16) must first be determined. Table 1 tabulates numerical values of these coefficients for four representative inhomogeneity indices. Values of other parameters are already given at the beginning of Section 3. It is also worth mentioning that, since the Young's modulus remains continuous across the shell-cylinder interface, its value does not enter into the determination of stress components.

Figure 4 shows the normalized radial stress along the thickness dimension of the structure for five inhomogeneity indices. It is found that the radial stress level can be effectively reduced by the use of an FGM shell. In particular, the radial stress at the graded shell-cylinder interface is significantly lower than that of an integral cylinder of constant stiffness. The larger the inhomogeneity index is the more effective the stress reduction becomes. Benefitting from the continuity of material properties across the graded shell-cylinder interface ( $r = r_0$ ), no sharp corners in the radial stress curves were observed. For all five cases, the maximum radial stress always appears at the outer surface of the cylinder and thus implies the absence of concentration.

To validate the accuracy of the developed analytical solution, finite element modelings of the exactly same model were also performed. Figure 5 shows the analytical solution and finite element results of the hoop stress distribution for five values of the inhomogeneity index. It can be seen that these two independent solutions agree with each other very well. In the finite element approach, the biggest challenge involves the modeling of the inhomogeneous shell. In this work, we closely followed a discretization

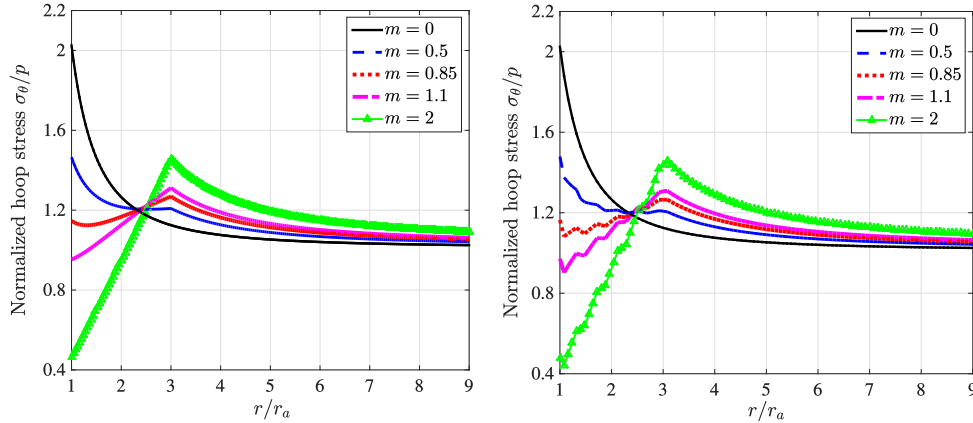


**Figure 5.** Variation of the normalized hoop stress along the radial dimension for five inhomogeneous shells. Left: analytical solution. Right: finite element modeling.

scheme recently proposed by Liu et al. [2018]. Readers who are interested in the numerical modeling of inhomogeneous materials may refer to the article for more details.

When compared with the radial stress, the distribution pattern of the hoop stress becomes more complicated. In the graded shell, three trends can be clearly observed. First, when  $m$  is small the hoop stress decreases all the way through the thickness of the shell. Second, as the value of the inhomogeneity index increases the hoop stress curve shows a parabolic behavior and a local minimum can be found somewhere between the shell rim and the shell-cylinder interface. Third, when the inhomogeneity index reaches a critical value (e.g.,  $m \approx 1.1$ ) the point of inflection of the hoop stress curve disappears and the hoop stress monotonically increases all the way through the thickness of the shell.

Similar to the case of a homogeneous inner shell, the hoop stress at the shell surface  $r = r_a$  decreases with increasing inhomogeneity index. However, the opposite trend is found at the shell-cylinder interface. On the other hand, the hoop stress within the outer cylinder decays all the way along the radial axis for any inhomogeneity index. Soft shells result in higher hoop stresses in the cylinder. Unlike the case of a homogeneous shell, the hoop stress across the shell-cylinder interface now becomes continuous but is still not differentiable. The sharpness of the corner at  $r = r_0$  behaves a positive function of the inhomogeneity index. It is clear that the maximum hoop stress for the case of an inhomogeneous shell may occur either at the shell rim or at the shell-cylinder interface, depending on the value of the inhomogeneity index. It can be inferred that there must exist an optimized inhomogeneity index ( $m = 0.731$ ) to make the hoop stress equal ( $\sigma_\theta/p = 1.248$ ) at the shell surface and at the shell-cylinder interface. It becomes obvious that the use of a graded inner shell is more effective than a homogeneous one when the stress reduction is of primary concern. In this case, the stress concentration factor has reduced by 38.4% when compared with a completely homogeneous thick-walled cylinder.

**3.2. An arbitrary biaxial traction load.** We now consider a thick-walled cylinder reinforced by a graded inner shell and subjected to a general biaxial traction load applied at the outer boundary of the cylinder. Since there are many possible combinations of the applied tractions  $p$  and  $q$ , we here introduce another parameter  $\gamma = q/p$ . In the numerical examples, several typical values of  $\gamma$  are taken, e.g.,  $\gamma = 1, 0.5, 0, -0.5$ , and  $-1$ . It is noted that when  $\gamma = 1$  the solution degenerates to the special case of

$z_{21}/p$	$z_{22}/p$	$z_{23}/p$	$z_{24}/p$	$D_1/p$	$D_2/p$	$D_3/p$	$D_4/p$
-0.272	$1.320 \cdot 10^{-04}$	-1.361	0.899	0.365	-0.189	-0.177	$3.485 \cdot 10^{-04}$

**Table 2.** Numerical values of the eight constants of integration in (25) that are used for plotting the various figures in Section 3.2. The other parameters are set as  $m = 0.5$ ,  $\nu = 0.3$ ,  $r_0/r_a = 3$ , and  $r_b/r_a = 9$ .

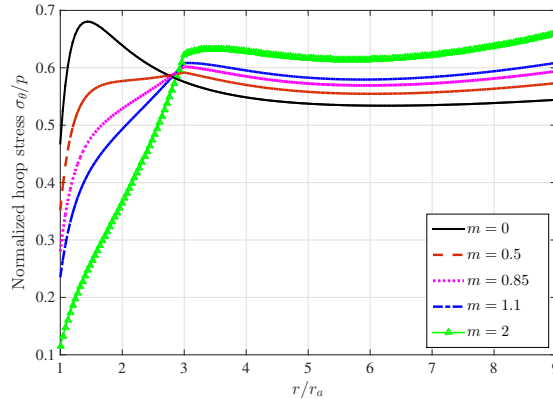


**Figure 6.** Variation of the normalized hoop stress along  $x$ -axis ( $\theta = 0$ ) for five inhomogeneity indices. The traction ratio was fixed as a constant  $\gamma = 0.5$ .

an axial symmetric traction load that was studied in the previous subsection. A uniaxial tension ( $\sigma_x = p$ ) is represented by  $\gamma = 0$  whereas the antisymmetric/pure shear load ( $\sigma_x = p, \sigma_y = -p$ ) is equivalent to  $\gamma = -1$ . Moreover, it is sufficient to consider the loading case of  $q \leq p$ , since all solutions due to  $q \geq p$  can be obtained by a simple coordinate rotation of  $\frac{1}{2}\pi$  around the axis of symmetry.

In addition to Table 1, calculation of stresses due to an arbitrary biaxial load also requires the eight constants of integration given by (25). For the representative inhomogeneity index  $m = 0.5$ , the numerical values of these coefficients are tabulated in Table 2. Again, stresses are independent on the Young’s modulus  $E^{(o)}$ , benefitting from its continuity across the shell-cylinder interface. In the next two subsections, we explore separately the effects of the inhomogeneity index  $m$  and the loading parameter  $\gamma$  on the stress reduction in the thick-walled cylinder.

**3.2.1. Effect of the inhomogeneity index.** In this subsection, we study the effect of the inhomogeneity index  $m$ . Several specific values of the index were considered in the subsequent numerical calculations, e.g.,  $m = 0, 0.5, 0.85, 1.1$ , and  $2$ . To exclude the undesired coupling effect of the traction ratio, it was fixed as a constant, i.e.,  $\gamma = 0.5$ , in this subsection.

Figures 6 and 7 show the hoop stress distribution along  $x$  and  $y$  directions, respectively. Along the radial direction  $\theta = 0$ , the behavior of the hoop stress has been significantly affected by the introduction of the inhomogeneous shell. For all cases with  $m \neq 0$ , the hoop stress now increases within the inner shell and then approximately stays constant in the cylinder. The location of the maximum hoop stress has changed from close to the inner surface of the shell toward to the shell-cylinder interface. Moreover, with increasing inhomogeneity the hoop stress value decreases at the inner surface of the shell. Slight fluctuations in the hoop stress level were found at the shell-cylinder boundary, with the highest stress

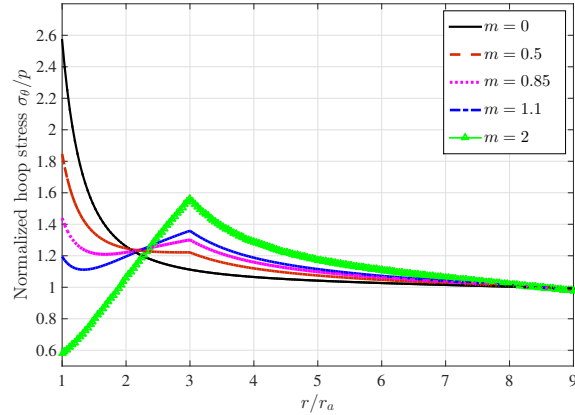


**Figure 7.** Variation of the normalized hoop stress along  $y$ -axis ( $\theta = \frac{1}{2}\pi$ ) for five inhomogeneity indices. The traction ratio was fixed as a constant  $\gamma = 0.5$ .

value given by the largest inhomogeneity  $m = 2$ . An intersection among the stress curves was found near the shell-cylinder interface, approaching from the shell side.

Along the other radial direction  $\theta = \frac{1}{2}\pi$ , the distribution of the hoop stress shows quite similar behavior as that of the case due to an all-around boundary traction (Figure 7). In the inhomogeneous shell, the hoop stress decreases when the shell inhomogeneity is small. In particular, for the special case of zero inhomogeneity ( $m = 0$ ), the stress concentration factor is the highest ( $\sigma_\theta/p = 2.556$ ). For large inhomogeneity indices, e.g.,  $m \geq 1.1$ , the trend has been reversed. Roughly in the interval  $0.85 < m < 1.1$ , the hoop stress curve behaves as a parabola with positive curvature and the maximum value of the hoop stress could occur on either boundary of the shell, or on both. In contrast, the hoop stresses in the outer cylinder monotonically decay for all values of the inhomogeneity index.

Referring to both Figure 6 and Figure 7, it can be concluded that the maximum hoop stress exists on either the inner surface of the shell or the shell-cylinder interface. Therefore, there must exist a critical inhomogeneity index,  $\hat{m}$ , which makes the hoop stress equal at  $r = r_a$  and  $r = r_0$ . A numerical search is performed for such an optimized inhomogeneity level. A close examination of Figures 6 and 7 reveals that the optimum inhomogeneity index must lie within the interval  $(0.85, 1.1)$ . The search can start from either the lower or the upper bound. For the given inhomogeneity index, the stress concentration factor at the inner surface of the shell is compared with that at the shell-cylinder interface. If the two factors are found to be unequal, the inhomogeneity index is updated by an increment of 0.001. The stress concentration factors are subsequently recalculated. The search stops until the difference between the two factors is less than a predefined degree of accuracy, e.g., 0.001. The final result was found to be  $\hat{m} \approx 0.961$ . It is clear that when  $m < \hat{m}$ , the maximum hoop stress occurs on the inner surface of the shell, the same situation as that of a completely homogeneous thick-walled cylinder. On the other hand, when  $m > \hat{m}$  the most severe stress concentration shifts to the shell-cylinder interface. The concentration factor of the hoop stress component reaches its minimum value ( $\sigma_\theta/p = 1.327$ ) when  $m = \hat{m}$ . This represents a reduction of 48.1% in the stress concentration factor when compared with a completely homogeneous cylinder under the exact same loading condition.



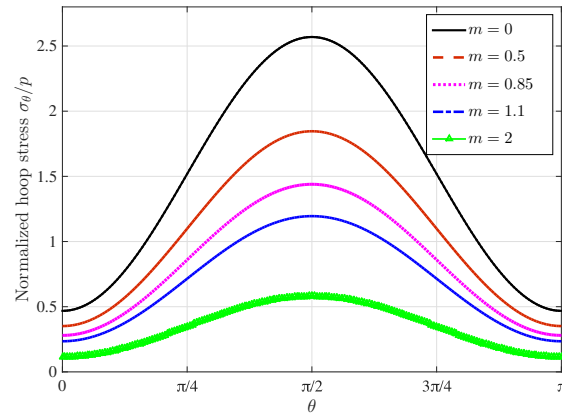


**Figure 8.** Variation of the normalized hoop stress along the inner surface of the inhomogeneous shell ( $r = r_a$ ) for five inhomogeneity indices. The traction ratio was fixed as a constant  $\gamma = 0.5$ .

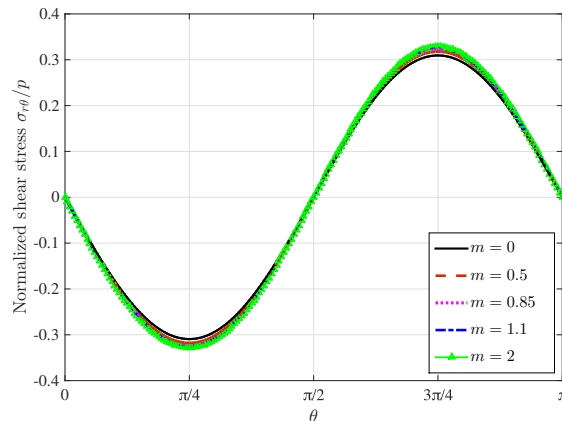


**Figure 9.** Variation of the normalized hoop stress along the shell-cylinder interface ( $r = r_0$ ) for five inhomogeneity indices. The traction ratio was fixed as a constant  $\gamma = 0.5$ .

Since the stress concentration always occurs on the inner surface for a cylinder subjected to far-field boundary loading, it is enlightening to examine the hoop stress distribution along  $r = r_a$ , as shown in Figure 8. It is seen that no matter how the inhomogeneity index changes, the hoop stress curve follows a complete period of sine-wave within  $\theta \in [0, \pi]$ . The minimum and the maximum hoop stresses are found at  $\theta = 0$  and  $\theta = \frac{1}{2}\pi$ , respectively. The general level of the hoop stress decreases with increasing inhomogeneity index.

Figure 9 shows the shear stress distribution along the shell-cylinder interface ( $r = r_0$ ). It is seen that the effect of the inhomogeneity index  $m$  is quite marginal. In the interval  $\theta \in [0, \pi]$ , all shear stress curves follow a complete sine-wave. The extremes of the shear stress appear at  $\theta = \frac{1}{4}\pi$  and  $\frac{3}{4}\pi$ . It is therefore instructive to examine the shear stress distribution along either of these two directions. Figure 10 shows the variation of the shear stress component through the wall thickness of the structure along  $\theta = \frac{1}{4}\pi$ . It is found that along this dimension all shear stresses are negative. A point of inflection exists for

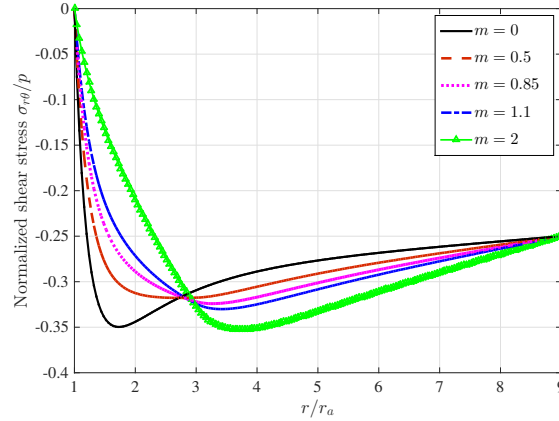


**Figure 10.** Variation of the normalized hoop stress along the radial direction ( $\theta = \frac{1}{4}\pi$ ) for five inhomogeneity indices. The traction ratio was fixed as a constant  $\gamma = 0.5$ .

all inhomogeneity indices, with the exact location clearly depending on the value of  $m$ . With increasing inhomogeneity index, the location of the shear stress extreme shifts from inside the inner shell to the outer cylinder. More importantly, the magnitude of the shear stress extreme decreases with the inhomogeneity index when  $m$  is small and subsequently increases when it becomes large. This observation implies that there exists an optimal inhomogeneity index  $\hat{m}$  at which the magnitude of the shear stress extreme assumes its lowest value. Numerical search suggests that the optimal inhomogeneity index is  $\hat{m} \approx 0.504$ , occurring at  $r \approx 2.767r_a$ . In this case, the corresponding concentration factor of the shear stress is the lowest ( $\sigma_{r\theta}/p = 0.318$ ).

**3.2.2. Effect of the traction ratio.** To investigate the effect of the traction ratio  $\gamma = q/p$ , in this subsection we fix the inhomogeneity index as a constant, i.e.,  $m = 0.5$ . As expected, for all loading cases ( $|\gamma| \leq 1$ ) no stress concentrations were found for the radial stress component. The absolute value of the maximum radial stress is never greater than  $p$ . It is therefore only necessary to examine the hoop and shear stresses.

The hoop stress distribution along the radial dimension  $\theta = 0$  is shown in Figure 11. It is seen that for positive  $\gamma$ , the hoop stress varies smoothly through the thickness of the structure. For negative  $\gamma$ , the hoop stress depends more sensitively on the radial coordinate. Very high compressive values are found near the inner surface of the graded shell whereas the stress curve varies quite smoothly in the outer cylinder. As  $\gamma$  switches from positive to negative, the hoop stress also switches from tension to compression. Again, excellent agreements have been achieved between the results predicted by the analytical approach and the finite element approach.

On the other hand, the distribution of the hoop stress along the radial direction  $\theta = \frac{1}{2}\pi$  behaves quite differently, as shown by both the analytical (Figure 12, left) and the finite element (Figure 12, right) solutions. In this direction, the hoop stress remains positive irrespective of the sign of the traction ratio  $\gamma$ . It is obvious that the hoop stress continuously decays in both domains, with a blunt corner found across the shell-cylinder interface. The level of  $\sigma_\theta$  in the inner shell is inversely proportional to  $\gamma$ . Although an opposite trend shows in the outer cylinder, the stress levels due to all loading conditions are actually quite close to  $\sigma_x = p$ . From Figure 12 it is clear that high stress concentrations appear near the inner surface of the embedded shell and the concentration factor increases with decreasing traction ratio  $\gamma$ .

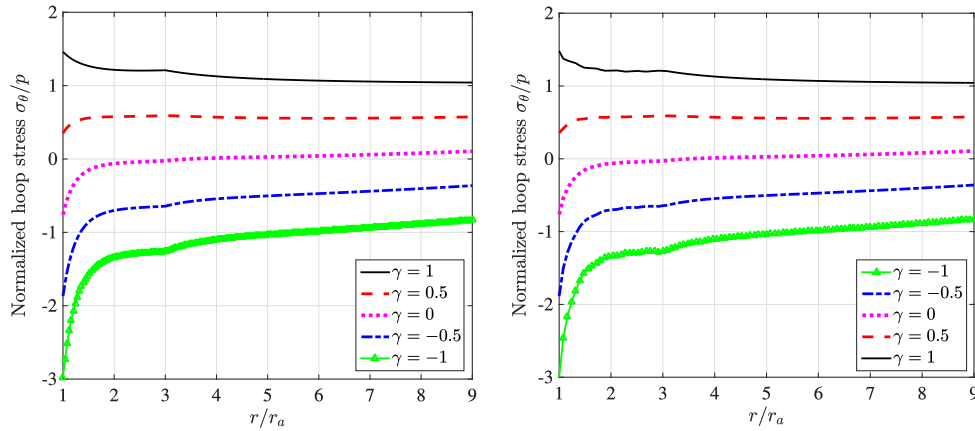


**Figure 11.** Variation of the normalized hoop stress along the  $x$  direction ( $\theta = 0$ ) for five boundary loads. The inhomogeneity index of the inner shell was fixed as a constant  $m = 0.5$ . Left: analytical solution. Right: finite element modeling.

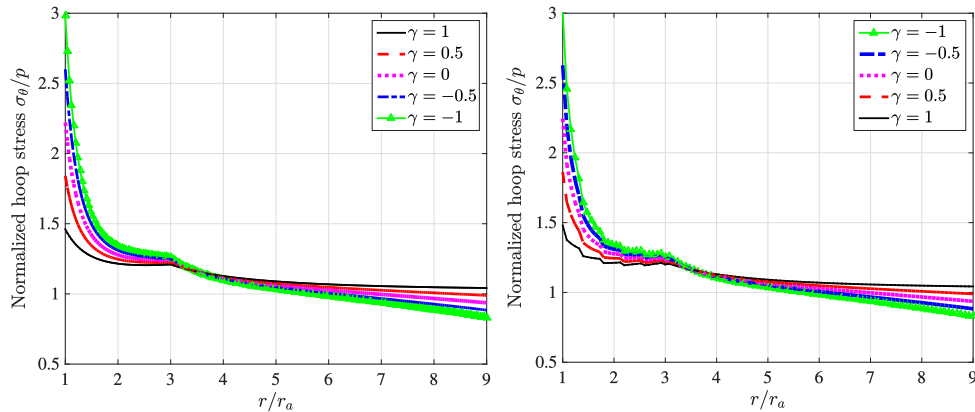


**Figure 12.** Variation of the normalized hoop stress along the  $y$  direction ( $\theta = \frac{1}{2}\pi$ ) for five boundary loads. The inhomogeneity index of the inner shell was fixed as a constant  $m = 0.5$ . Left: analytical solution. Right: finite element modeling.

Informed by Figures 11 and 12, high stress values are always found at the surface of the inner shell. As a result, in Figure 13, we present the distribution of the hoop stress along the inner surface of the shell  $r = r_a$ . Due to symmetry, only a half interval of the surface was taken into account. In general, for  $\theta \in [0, \pi]$ , the hoop stress varies by following a sine pattern for each traction ratio  $\gamma$ . It is found that stress extremes always appear along the  $x$  or  $y$  direction. For all traction ratios considered in the numerical study ( $|\gamma| \leq 1$ ), the maximum compressive and tensile hoop stresses happen along the  $x$  and  $y$  direction, respectively. Among them, the antisymmetric traction load results in the highest stress concentration factor ( $\sigma_\theta/p = 3$ ), the same value as that of a voided homogeneous plate subjected to a uniaxial tensile load. Nonetheless, it should be recalled that such a stress distribution is obtained by fixing the inhomogeneity index of the inner shell as a constant ( $m = 0.5$ ).

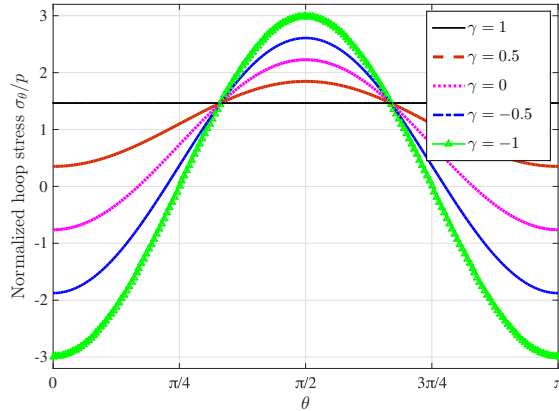


**Figure 13.** Variation of the normalized hoop stress along the inner surface of the shell ( $r = r_a$ ) for five boundary loads. The inhomogeneity index of the inner shell was fixed as a constant  $m = 0.5$ .

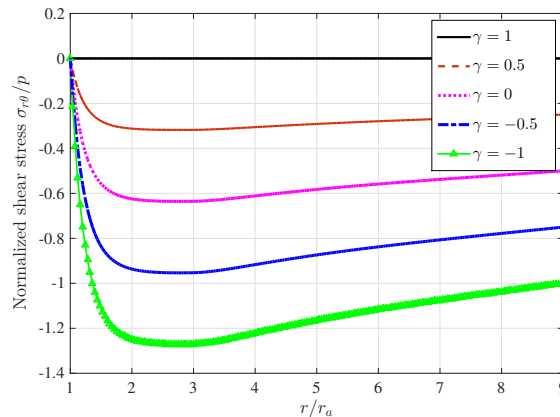


**Figure 14.** Variation of the normalized shear stress along the radial direction ( $\theta = \frac{1}{4}\pi$ ) for five boundary loads. The inhomogeneity index of the inner shell was fixed as a constant  $m = 0.5$ .

Enlightened by the stress distribution in an axially loaded structural member, the maximum shear stress should occur along the radial direction  $\theta = \frac{1}{4}\pi$ , as shown in Figure 14. The magnitude of the shear stress increases with decreasing  $\gamma$ , as the boundary loading shifts from an all-around tension to an antisymmetric load. For the case of  $\gamma = -1$ , slight stress concentration in the shear stress component was found near the shell-cylinder interface. Along the radial direction, the absolute value of the shear stress rapidly increases in the inner half of the shell and remains nearly constant in the outer half. No significant variations of the shear stress occur in the cylinder.

Figure 15 shows the distribution of the shear stress component along the shell-cylinder interface ( $r = r_0$ ). As can be expected, the maximum values are found along directions that are  $\frac{1}{4}\pi$  from the two loading axes ( $\theta = 0, \frac{1}{2}\pi$ ). The shear stress extremes behave a negative function of the traction ratio  $\gamma$ , with the maximum values occurring in the case of the antisymmetric load.

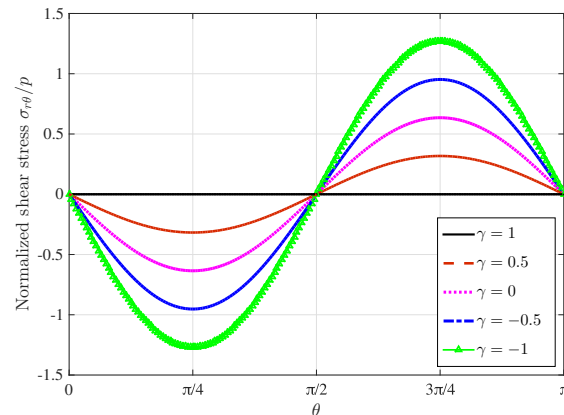


**Figure 15.** Variation of the normalized shear stress along the shell-cylinder interface ( $r = r_0$ ) for five boundary loads. The inhomogeneity index of the inner shell was fixed as a constant  $m = 0.5$ .

#### 4. Conclusions

In this work, we solved the stress distribution and stress concentration in a homogeneous thick-walled cylinder, reinforced by either a radially graded or a homogeneous inner shell. An arbitrary biaxial traction load applied at the outer boundary of the cylinder was taken into consideration. Closed-form analytical solutions were obtained with the method of Airy stress function. On the basis of the analytical solutions and extensive numerical experiments, a few summaries and conclusions can be made as follows:

- We show that the stress concentration that is commonly encountered in thick-walled cylinders can be significantly mitigated by introducing a graded inner shell with a proper distribution in elastic modulus.
- With reference to the elastic stiffness of a thick-walled cylinder, a graded soft shell tends to decrease the conventional stress concentration occurring at the inner boundary of the structure. Nonetheless, stresses at the interface separating the shell and the cylinder increase inevitably due to the softening of the inner layer of the hollow structure.
- An optimal inhomogeneity index in the power-law gradation can be found for which the stress concentrations at the inner boundary of the structure and at the shell-cylinder interface are well balanced.
- In addition to the inhomogeneity index of the embedded shell, we also investigated the effect of the biaxial traction ratio. For all loading cases, no significant concentrations in the radial and shear stress components are found. The hoop stress concentration is therefore of the primary concern. In analogy to the classical solution of a thick-walled cylinder, the concentration factor in the hoop stress component increases with growing difference (including sign) between the boundary loads along perpendicular directions. In this sense, an all-around uniform load is most desired.

Despite the completeness of this work in the context of an idealized plane elasticity problem, future work in this line of research could entail more practical engineering conditions:

- (1) the incorporation of more realistic bonding conditions across the embedded shell-cylinder interface,
- (2) grading functions different than the power-law, and
- (3) three-dimensional structures.

### Appendix: Expressions for the various parameters defined in (25)

The parameters  $\lambda_{ij}$ ,  $\eta_{ij}$ ,  $\mu_{ij}$ , and  $\psi_{ij}$  are elements of four  $4 \times 4$  matrices:

$$\lambda_{11} = \frac{1}{\Lambda A_1(r_0)} \left( 4(1+\nu)\beta M_{22} + 2(1+\nu)(\alpha - \beta)M_{23} - 2(1+\nu)(\alpha + \beta)M_{24} \right. \\ \left. + M_{14}(2(1+\nu)(\alpha - \beta) + (2 - m + \beta)M_{22} + (-2 + m + \alpha)M_{23}) \right. \\ \left. + M_{13}(-2(1+\nu)(\alpha - \beta) + (-2 + m + \beta)M_{22} + (2 - m - \alpha)M_{24}) \right. \\ \left. + M_{12}(-4(1+\nu)\beta + (2 - m - \beta)M_{23} + (-2 + m - \beta)M_{24}) \right),$$

$$\lambda_{12} = \frac{1}{\Lambda A_1(r_0)} \left( 8\nu\beta M_{22} + 4\nu(\alpha - \beta)M_{23} - 4\nu(\alpha + \beta)M_{24} \right. \\ \left. + M_{14}(2(3+\nu)(\alpha + \beta) + (6 - m + \beta)M_{22} + (m - 6 + \alpha)M_{23}) \right. \\ \left. + M_{13}(-2(3+\nu)(\alpha - \beta) + (m - 6 + \beta)M_{22} + (6 - m - \alpha)M_{24}) \right. \\ \left. + M_{12}((6 - m - \beta)M_{23} - 4(3+\nu)\beta + (m - 6 - \beta)M_{24}) \right),$$

$$\lambda_{13} = \frac{1}{\Lambda A_1(r_0)} \left( 2(1+\nu)(\alpha + \beta)M_{24} - 4(1+\nu)\beta M_{22} - 2(1+\nu)(\alpha - \beta)M_{23} \right. \\ \left. + M_{14}(2(1+\nu)(\alpha + \beta) + (\beta - 6 - m)M_{22} + (6 + m + \alpha)M_{23}) \right. \\ \left. + M_{13}((6 + m + \beta)M_{22} - 2(1+\nu)(\alpha - \beta) - (6 + m + \alpha)M_{24}) \right. \\ \left. + M_{12}((6 + m - \beta)M_{24} - 4(1+\nu)\beta - (6 + m + \beta)M_{23}) \right),$$

$$\lambda_{14} = \frac{1}{\Lambda A_1(r_0)} \left( 4(\alpha + \beta)M_{24} - 8\beta M_{22} + 4(\beta - \alpha)M_{23} \right. \\ \left. + M_{14}(2(\nu - 1)(\alpha + \beta) + (\beta - 2 - m)M_{22} + (2 + m + \alpha)M_{23}) \right. \\ \left. + M_{13}(2(1 - \nu)(\alpha - \beta) + (2 + m + \beta)M_{22} - (2 + m + \alpha)M_{24}) \right. \\ \left. + M_{12}(4(1 - \nu)\beta - (2 + m + \beta)M_{23} + (2 + m - \beta)M_{24}) \right),$$

$$\lambda_{21} = \frac{1}{\Lambda A_2(r_0)} \left( 2(1+\nu)(\alpha + \beta)M_{23} - 4(1+\nu)\beta M_{21} - 2(1+\nu)(\alpha - \beta)M_{24} \right. \\ \left. + M_{14}(2(1+\nu)(\alpha - \beta) + (m - 2 - \beta)M_{21} + (2 - m + \alpha)M_{23}) \right. \\ \left. + M_{13}((2 - m - \beta)M_{21} - 2(1+\nu)(\alpha + \beta) + (m - 2 - \alpha)M_{24}) \right. \\ \left. + M_{11}(4(1+\nu)\beta + (m - 2 + \beta)M_{23} + (2 - m + \beta)M_{24}) \right),$$

$$\lambda_{22} = \frac{1}{\Lambda A_2(r_0)} \left( 4\nu(\alpha + \beta)M_{23} - 8\nu\beta M_{21} - 4\nu(\alpha - \beta)M_{24} \right. \\ \left. + M_{14}(2(3+\nu)(\alpha - \beta) + (m - 6 - \beta)M_{21} + (6 - m + \alpha)M_{23}) \right. \\ \left. + M_{13}((6 - m - \beta)M_{21} - 2(3+\nu)(\alpha + \beta) + (m - 6 - \alpha)M_{24}) \right. \\ \left. + M_{11}(4(3+\nu)\beta + (m - 6 + \beta)M_{23} + (6 - m + \beta)M_{24}) \right),$$

$$\begin{aligned} \lambda_{23} &= \frac{1}{\Lambda A_2(r_0)} \left( 4(1+\nu)\beta M_{21} - 2(1+\nu)(\alpha + \beta)M_{23} + 2(1+\nu)(\alpha - \beta)M_{24} \right. \\ &\quad + M_{14}(2(1+\nu)(\alpha - \beta) + (6+m-\beta)M_{21} + (\alpha - 6 - m)M_{23}) \\ &\quad + M_{13}((6+m-\alpha)M_{24} - 2(1+\nu)(\alpha + \beta) - (6+m+\beta)M_{21}) \\ &\quad \left. + M_{11}(4(1+\nu)\beta + (6+m+\beta)M_{23} + (\beta - 6 - m)M_{24}) \right), \\ \lambda_{24} &= \frac{1}{\Lambda A_2(r_0)} \left( 8\beta M_{21} - 4(\alpha + \beta)M_{23} + 4\nu(\alpha - \beta)M_{24} \right. \\ &\quad + M_{14}(2(\nu - 1)(\alpha - \beta) + (2+m-\beta)M_{21} + (\alpha - 2 - m)M_{23}) \\ &\quad + M_{13}(2(1-\nu)(\alpha + \beta) - (2+m+\beta)M_{21} + (2+m-\alpha)M_{24}) \\ &\quad \left. + M_{11}(4(\nu - 1)\beta + (2+m+\beta)M_{23} + (2-m+\beta)M_{24}) \right), \\ \lambda_{31} &= \frac{1}{\Lambda B_1(r_0)} \left( -2(1+\nu)(\alpha - \beta)M_{21} + 2(1+\nu)(\alpha + \beta)M_{22} + 4(1+\nu)\alpha M_{24} \right. \\ &\quad + M_{14}((2-m-\alpha)M_{21} - 4(1+\nu)\alpha + (m-2-\alpha)M_{22}) \\ &\quad + M_{12}(2(1+\nu)(\alpha + \beta) + (m-2+\beta)M_{21} + (2-m+\alpha)M_{24}) \\ &\quad \left. + M_{11}(2(1+\nu)(\alpha - \beta) + (2-m-\beta)M_{22} + (m-2+\alpha)M_{24}) \right), \\ \lambda_{32} &= \frac{1}{\Lambda B_1(r_0)} \left( 8\nu\alpha M_{24} - 4\nu(\alpha - \beta)M_{21} - 4\nu(\alpha + \beta)M_{22} \right. \\ &\quad + M_{14}((6-m-\alpha)M_{21} - 4(3+\nu)\alpha + (m-6-\alpha)M_{22}) \\ &\quad + M_{12}(2(3+\nu)(\alpha + \beta) + (m-6+\beta)M_{21} + (6-m+\alpha)M_{24}) \\ &\quad \left. + M_{11}(2(3+\nu)(\alpha - \beta) + (6-m-\beta)M_{22} + (m-6+\alpha)M_{24}) \right), \\ \lambda_{33} &= \frac{1}{\Lambda B_1(r_0)} \left( 2(1+\nu)(\alpha - \beta)M_{21} + 2(1+\nu)(\alpha + \beta)M_{22} + 4(1+\nu)\alpha M_{24} \right. \\ &\quad + M_{14}((6+m-\alpha)M_{22} - 4(1+\nu)\alpha - (6+m+\alpha)M_{21}) \\ &\quad + M_{12}(2(1+\nu)(\alpha + \beta) + (6+m+\beta)M_{21} + (\alpha - 6 - m)M_{24}) \\ &\quad \left. + M_{11}(2(1+\nu)(\alpha - \beta) - (6+m+\beta)M_{22} + (6+m+\alpha)M_{24}) \right), \\ \lambda_{34} &= \frac{1}{\Lambda B_1(r_0)} \left( 4(\alpha - \beta)M_{21} + 4(\alpha + \beta)M_{22} - 8\alpha M_{24} \right. \\ &\quad + M_{14}(4(1-\nu)\alpha - (2+m+\alpha)M_{21} + (2+m-\alpha)M_{22}) \\ &\quad + M_{12}(2(\nu - 1)(\alpha + \beta) + (2+m+\beta)M_{21} + (\alpha - 2 - m)M_{24}) \\ &\quad \left. + M_{11}(2(\nu - 1)(\alpha - \beta) - (2+m+\beta)M_{22} + (2+m+\alpha)M_{24}) \right), \\ \lambda_{41} &= \frac{1}{\Lambda B_2(r_0)} \left( 2(1+\nu)(\alpha + \beta)M_{21} + 2(1+\nu)(\alpha - \beta)M_{22} - 4(1+\nu)\alpha M_{23} \right. \\ &\quad + M_{13}(4(1+\nu)\alpha + (m-2+\alpha)M_{21} + (2-m+\alpha)M_{22}) \\ &\quad + M_{11}((m-2-\beta)M_{22} - 2(1+\nu)(\alpha + \beta) + (2-m-\alpha)M_{23}) \\ &\quad \left. + M_{12}((2-m+\beta)M_{21} - 2(1+\nu)(\alpha - \beta) + (m-2-\alpha)M_{23}) \right), \end{aligned}$$

$$\lambda_{42} = \frac{1}{\Lambda B_2(r_0)} \left( 4v(\alpha + \beta)M_{21} + 4v(\alpha - \beta)M_{22} - 8v\alpha M_{23} \right. \\ \left. + M_{13}(4(3 + v)\alpha + (m - 6 + \alpha)M_{21} + (6 - m + \alpha)M_{22}) \right. \\ \left. + M_{11}((m - 6 - \beta)M_{22} - 2(3 + v)(\alpha + \beta) + (6 - m - \alpha)M_{23}) \right. \\ \left. + M_{12}((6 - m + \beta)M_{21} - 2(3 + v)(\alpha - \beta) + (m - 6 - \alpha)M_{23}) \right),$$

$$\lambda_{43} = \frac{1}{\Lambda B_2(r_0)} \left( 4(1 + v)\alpha M_{23} - 2(1 + v)(\alpha + \beta)M_{21} - 2(1 + v)(\alpha - \beta)M_{22} \right. \\ \left. + M_{13}(4(1 + v)\alpha + (6 + m + \alpha)M_{21} + (\alpha - 6 - m)M_{22}) \right. \\ \left. + M_{11}((6 + m - \beta)M_{22} - 2(1 + v)(\alpha + \beta) - (6 + m + \alpha)M_{23}) \right. \\ \left. + M_{12}((\beta - 6 - m)M_{21} - 2(1 + v)(\alpha - \beta) + (6 + m - \alpha)M_{23}) \right),$$

$$\lambda_{44} = \frac{1}{\Lambda B_2(r_0)} \left( 8\alpha M_{23} - 4(\alpha + \beta)M_{21} - 4v(\alpha - \beta)M_{22} \right. \\ \left. + M_{13}(4(v - 1)\alpha + (2 + m + \alpha)M_{21} + (\alpha - 2 - m)M_{22}) \right. \\ \left. + M_{11}(2(1 - v)(\alpha + \beta) + (2 + m - \beta)M_{22} - (2 + m + \alpha)M_{23}) \right. \\ \left. + M_{12}(2(1 - v)(\alpha - \beta) + (\beta - 2 - m)M_{21} + (2 + m - \alpha)M_{23}) \right),$$

$$\eta_{ij} = r_b^2 r_0^4 (\lambda_{i3} \lambda_{j2} - \lambda_{j3} \lambda_{i2}) + 2r_0^6 (\lambda_{i2} \lambda_{j4} - \lambda_{j2} \lambda_{i4}) + r_b^6 (\lambda_{i3} \lambda_{j4} - \lambda_{j3} \lambda_{i4}),$$

$$\mu_{ij} = r_0^4 (\lambda_{i2} \lambda_{j1} - \lambda_{j2} \lambda_{i1}) + r_b^4 (\lambda_{i4} \lambda_{j1} - \lambda_{j4} \lambda_{i1}),$$

$$\psi_{ij} = r_0^8 (\lambda_{i2} \lambda_{j1} - \lambda_{j2} \lambda_{i1}) + 2r_b^2 r_0^6 (\lambda_{i4} \lambda_{j2} - \lambda_{i2} \lambda_{j4}) + r_b^4 r_0^4 (3(\lambda_{i1} \lambda_{j4} - \lambda_{i4} \lambda_{j1}) + \lambda_{i2} \lambda_{j3} - \lambda_{i3} \lambda_{j2}) \\ + 2r_b^6 r_0^2 (\lambda_{i3} \lambda_{j1} - \lambda_{i1} \lambda_{j3}) + r_b^8 (\lambda_{i4} \lambda_{j3} - \lambda_{j4} \lambda_{i3}),$$

where

$$M_{11} = \frac{(m^2 + 2(1 - \alpha)m - \alpha(2 - \alpha))v}{2(m + \alpha)} - \frac{m - \alpha - 6}{m + \alpha},$$

$$M_{12} = \frac{(m^2 + 2(1 + \alpha)m + \alpha(2 + \alpha))v}{2(m - \alpha)} - \frac{m + \alpha - 6}{m - \alpha},$$

$$M_{13} = \frac{(m^2 + 2(1 - \beta)m - \beta(2 - \beta))v}{2(m + \beta)} - \frac{m - \beta - 6}{m + \beta},$$

$$M_{14} = \frac{(m^2 + 2(1 + \beta)m + \beta(2 + \beta))v}{2(m - \beta)} - \frac{m + \beta - 6}{m - \beta},$$

$$M_{21} = \frac{1}{96} (m^2(4v - 28) + m(\beta^2 - \alpha^2 + 28\beta - 4\beta v - 24v - 88) \\ - \beta^3 - 6\beta^2 + 6\alpha^2 + \alpha^2\beta + 64\beta - 192v - 192),$$

$$M_{22} = \frac{1}{96} (m^2(4v - 28) + m(\alpha^2 - \beta^2 - 28\alpha - 4\alpha v - 24v - 88) \\ + \alpha^3 - 6\alpha^2 + 6\beta^2 - \beta^2\alpha - 64\alpha - 192v - 192),$$



$$M_{23} = \frac{1}{96}(m^2(4\nu - 28) - m(\alpha^2 - \beta^2 + 28\beta - 4\beta\nu + 24\nu + 88) \\ + \beta^3 - 6\beta^2 + 6\alpha^2 - \alpha^2\beta - 64\beta - 192\nu - 192),$$

$$M_{24} = \frac{1}{96}(m^2(4\nu - 28) - m(\beta^2 - \alpha^2 - 28\alpha + 4\alpha\nu + 24\nu + 88) \\ + \alpha^3 + 6\alpha^2 - 6\beta^2 - \beta^2\alpha - 64\alpha + 192\nu + 192),$$

and

$$\Lambda = M_{11}(-2\beta M_{22} - (\alpha - \beta)M_{23} + (\alpha + \beta)M_{24}) + M_{12}(2\beta M_{21} - (\alpha + \beta)M_{23} + (\alpha - \beta)M_{24}) \\ + M_{13}((\alpha - \beta)M_{21} + (\alpha + \beta)M_{22} - 2\alpha M_{24}) + M_{14}(-(\alpha + \beta)M_{21} - (\alpha - \beta)M_{22} + 2\alpha M_{23}).$$

The parameters  $\xi_i$ ,  $a_i$ , and  $\zeta_i$  are elements of three four-component vectors

$$\xi_i = \{\alpha \quad -\alpha \quad \beta \quad -\beta\},$$

$$a_i = \{A_1(r_a) \quad A_2(r_a) \quad B_1(r_a) \quad B_2(r_a)\},$$

$$\zeta_i = \{r_0^{1-m} \quad r_0^{3-m} \quad r_0^{-3-m} \quad r_0^{-1-m}\}.$$

### Acknowledgements

This work was supported by the National Natural Science Foundation of China (grant numbers: 11702076 and 11472079), the National Key R&D Program of China (grant number 2017YFC0702800), the Natural Science Foundation of Jiangsu Province (grant number BK20161411), and the Fundamental Research Funds for the Central Universities.

### References

- [Barber 2010] J. R. Barber, *Elasticity*, 3rd ed., Solid Mechanics and Its Applications **172**, Springer, 2010.
- [Batista 2011] M. Batista, "On the stress concentration around a hole in an infinite plate subject to a uniform load at infinity", *Int. J. Mech. Sci.* **53**:4 (2011), 254–261.
- [Batra and Nie 2010] R. C. Batra and G. J. Nie, "Analytical solutions for functionally graded incompressible eccentric and non-axisymmetrically loaded circular cylinders", *Compos. Struct.* **92**:5 (2010), 1229–1245.
- [Birman and Byrd 2007] V. Birman and L. W. Byrd, "Modeling and analysis of functionally graded materials and structures", *Appl. Mech. Rev. (ASME)* **60**:5 (2007), 195–216.
- [Chen 2015] Y. Z. Chen, "A novel solution for thick-walled cylinders made of functionally graded materials", *Smart Struct. Syst.* **15**:6 (2015), 1503–1520.
- [Chen and Lin 2010] Y. Z. Chen and X. Y. Lin, "An alternative numerical solution of thick-walled cylinders and spheres made of functionally graded materials", *Comput. Mater. Sci.* **48**:3 (2010), 640–647.
- [Chen et al. 2012] X. Chen, L. Gu, B. Zou, Y. Wang, and X. Cao, "New functionally graded thermal barrier coating system based on LaMgAl<sub>11</sub>O<sub>19</sub>/YSZ prepared by air plasma spraying", *Surf. Coat. Technol.* **206**:8-9 (2012), 2265–2274.
- [Chi and Chung 2006a] S.-H. Chi and Y.-L. Chung, "Mechanical behavior of functionally graded material plates under transverse load, I: Analysis", *Int. J. Solids Struct.* **43**:13 (2006), 3657–3674.
- [Chi and Chung 2006b] S.-H. Chi and Y.-L. Chung, "Mechanical behavior of functionally graded material plates under transverse load, II: Numerical results", *Int. J. Solids Struct.* **43**:13 (2006), 3675–3691. Correction in **44**:5 (2007), 1691.
- [Chu et al. 2015] P. Chu, X.-F. Li, J.-X. Wu, and K. Y. Lee, "Two-dimensional elasticity solution of elastic strips and beams made of functionally graded materials under tension and bending", *Acta Mech.* **226**:7 (2015), 2235–2253.

- [Dryden and Batra 2013] J. Dryden and R. C. Batra, “Optimum Young’s modulus of a homogeneous cylinder energetically equivalent to a functionally graded cylinder”, *J. Elasticity* **110**:1 (2013), 95–110.
- [Ghannad et al. 2013] M. Ghannad, G. H. Rahimi, and M. Z. Nejad, “Elastic analysis of pressurized thick cylindrical shells with variable thickness made of functionally graded materials”, *Compos. B Eng.* **45**:1 (2013), 388–396.
- [Gouasmi et al. 2015] S. Gouasmi, A. Megueni, A. S. Bouchikhi, K. Zouggar, and A. Sahli, “On the reduction of stress concentration factor around a notch using a functionally graded layer”, *Mater. Res.* **18**:5 (2015), 971–977.
- [Horgan and Chan 1999] C. O. Horgan and A. M. Chan, “The pressurized hollow cylinder or disk problem for functionally graded isotropic linearly elastic materials”, *J. Elasticity* **55**:1 (1999), 43–59.
- [Jha et al. 2013] D. K. Jha, T. Kant, and R. K. Singh, “A critical review of recent research on functionally graded plates”, *Compos. Struct.* **96** (2013), 833–849.
- [Jin and Batra 1996] Z.-H. Jin and R. C. Batra, “Some basic fracture mechanics concepts in functionally graded materials”, *J. Mech. Phys. Solids* **44**:8 (1996), 1221–1235.
- [Kashtalyan and Menshykova 2007] M. Kashtalyan and M. Menshykova, “Three-dimensional elastic deformation of a functionally graded coating/substrate system”, *Int. J. Solids Struct.* **44**:16 (2007), 5272–5288.
- [Kawasaki and Watanabe 2002] A. Kawasaki and R. Watanabe, “Thermal fracture behavior of metal/ceramic functionally graded materials”, *Eng. Fract. Mech.* **69**:14-16 (2002), 1713–1728.
- [Kubair 2013] D. V. Kubair, “Stress concentration factors and stress-gradients due to circular holes in radially functionally graded panels subjected to anti-plane shear loading”, *Acta Mech.* **224**:11 (2013), 2845–2862.
- [Kubair and Bhanu-Chandar 2008] D. V. Kubair and B. Bhanu-Chandar, “Stress concentration factor due to a circular hole in functionally graded panels under uniaxial tension”, *Int. J. Mech. Sci.* **50**:4 (2008), 732–742.
- [Liu et al. 2018] Z. Liu, J. Yan, and C. Mi, “On the receding contact between a two-layer inhomogeneous laminate and a half-plane”, *Struct. Eng. Mech.* **66**:3 (2018), 329–341.
- [Marin 2005] L. Marin, “Numerical solution of the Cauchy problem for steady-state heat transfer in two-dimensional functionally graded materials”, *Int. J. Solids Struct.* **42**:15 (2005), 4338–4351.
- [Mohammadi et al. 2011] M. Mohammadi, J. R. Dryden, and L. Jiang, “Stress concentration around a hole in a radially inhomogeneous plate”, *Int. J. Solids Struct.* **48**:3-4 (2011), 483–491.
- [Mohammadi et al. 2016] M. Mohammadi, G. C. Saha, and A. H. Akbarzadeh, “Elastic field in composite cylinders made of functionally graded coatings”, *Int. J. Eng. Sci.* **101** (2016), 156–170.
- [Müller et al. 2003] E. Müller, Č. Drásar, J. Schilz, and W. A. Kaysser, “Functionally graded materials for sensor and energy applications”, *Mater. Sci. Eng. A* **362**:1-2 (2003), 17–39.
- [Nagpal et al. 2012] S. Nagpal, N. Jain, and S. Sanyal, “Stress concentration and its mitigation techniques in flat plate with singularities: a critical review”, *Eng. J.* **16**:1 (2012), 1–16.
- [Nie and Batra 2010] G. J. Nie and R. C. Batra, “Exact solutions and material tailoring for functionally graded hollow circular cylinders”, *J. Elasticity* **99**:2 (2010), 179–201.
- [Nie et al. 2011] G. J. Nie, Z. Zhong, and R. C. Batra, “Material tailoring for functionally graded hollow cylinders and spheres”, *Compos. Sci. Technol.* **71**:5 (2011), 666–673.
- [Oral and Anlas 2005] A. Oral and G. Anlas, “Effects of radially varying moduli on stress distribution of nonhomogeneous anisotropic cylindrical bodies”, *Int. J. Solids Struct.* **42**:20 (2005), 5568–5588.
- [Pan and Roy 2006] E. Pan and A. K. Roy, “A simple plane-strain solution for functionally graded multilayered isotropic cylinders”, *Struct. Eng. Mech.* **24**:6 (2006), 727–740.
- [Patel and Sharma 2017] N. P. Patel and D. S. Sharma, “On the stress concentration around a polygonal cut-out of complex geometry in an infinite orthotropic plate”, *Compos. Struct.* **179** (2017), 415–436.
- [Rezaeepazhand and Jafari 2010] J. Rezaeepazhand and M. Jafari, “Stress concentration in metallic plates with special shaped cutout”, *Int. J. Mech. Sci.* **52**:1 (2010), 96–102.
- [Sadeghi et al. 2012] H. Sadeghi, M. Baghani, and R. Naghdabadi, “Strain gradient elasticity solution for functionally graded micro-cylinders”, *Int. J. Eng. Sci.* **50**:1 (2012), 22–30.

- [Savin 1961] G. N. Savin, *Stress concentration around holes*, International Series of Monographs on Aeronautics and Astronautics, Division I: Solid and Structural Mechanics **1**, Pergamon, New York, 1961.
- [Sburlati 2012] R. Sburlati, “Analytical elastic solutions for pressurized hollow cylinders with internal functionally graded coatings”, *Compos. Struct.* **94**:12 (2012), 3592–3600.
- [Sburlati 2013] R. Sburlati, “Stress concentration factor due to a functionally graded ring around a hole in an isotropic plate”, *Int. J. Solids Struct.* **50**:22-23 (2013), 3649–3658.
- [Sburlati et al. 2013] R. Sburlati, S. R. Atashipour, and S. Hosseini-Hashemi, “Study on the effect of functionally graded coating layers on elastic deformation of thick circular plates: a closed-form elasticity solution”, *Compos. Struct.* **99** (2013), 131–140.
- [Sburlati et al. 2014] R. Sburlati, S. R. Atashipour, and S. A. Atashipour, “Reduction of the stress concentration factor in a homogeneous panel with hole by using a functionally graded layer”, *Compos. B Eng.* **61** (2014), 99–109.
- [Theocaris and Petrou 1986] P. S. Theocaris and L. Petrou, “Stress distributions and intensities at corners of equilateral triangular holes”, *Int. J. Fract.* **31**:4 (1986), 271–289.
- [Tutuncu 2007] N. Tutuncu, “Stresses in thick-walled FGM cylinders with exponentially-varying properties”, *Eng. Struct.* **29**:9 (2007), 2032–2035.
- [Ukadgaonker and Rao 1999] V. G. Ukadgaonker and D. K. N. Rao, “Stress distribution around triangular holes in anisotropic plates”, *Compos. Struct.* **45**:3 (1999), 171–183.
- [Watari et al. 2004] F. Watari, A. Yokoyama, M. Omori, T. Hirai, H. Kondo, M. Uo, and T. Kawasaki, “Biocompatibility of materials and development to functionally graded implant for bio-medical application”, *Compos. Sci. Technol.* **64**:6 (2004), 893–908.
- [Wu and Mu 2003] H.-C. Wu and B. Mu, “On stress concentrations for isotropic/orthotropic plates and cylinders with a circular hole”, *Compos. B Eng.* **34**:2 (2003), 127–134.
- [Xin et al. 2014] L. Xin, G. Dui, S. Yang, and J. Zhang, “An elasticity solution for functionally graded thick-walled tube subjected to internal pressure”, *Int. J. Mech. Sci.* **89** (2014), 344–349.
- [Yang and Gao 2016] Q. Yang and C.-F. Gao, “Reduction of the stress concentration around an elliptic hole by using a functionally graded layer”, *Acta Mech.* **227**:9 (2016), 2427–2437.
- [Yang et al. 2008] Z. Yang, C.-B. Kim, C. Cho, and H. G. Beom, “The concentration of stress and strain in finite thickness elastic plate containing a circular hole”, *Int. J. Solids Struct.* **45**:3-4 (2008), 713–731.
- [Yang et al. 2010a] Q. Yang, C.-F. Gao, and W. Chen, “Stress analysis of a functional graded material plate with a circular hole”, *Arch. Appl. Mech.* **80**:8 (2010), 895–907.
- [Yang et al. 2010b] Z. Yang, C.-B. Kim, H. G. Beom, and C. Cho, “The stress and strain concentrations of out-of-plane bending plate containing a circular hole”, *Int. J. Mech. Sci.* **52**:6 (2010), 836–846.
- [Yang et al. 2015] B. Yang, W. Q. Chen, and H. J. Ding, “3D elasticity solutions for equilibrium problems of transversely isotropic FGM plates with holes”, *Acta Mech.* **226**:5 (2015), 1571–1590.

Received 26 Dec 2017. Revised 10 May 2018. Accepted 27 May 2018.

XIAOBAO LI: xiaobaoli@hfut.edu.cn

School of Civil Engineering, Hefei University of Technology, Hefei, China

YIWEI HUA: 107653759@qq.com

Jiangsu Key Laboratory of Engineering Mechanics, School of Civil Engineering, Southeast University, Nanjing, China

CHENYI ZHENG: 594040623@qq.com

Jiangsu Key Laboratory of Engineering Mechanics, School of Civil Engineering, Southeast University, Nanjing, China

CHANGWEN MI: mi@seu.edu.cn

Jiangsu Key Laboratory of Engineering Mechanics, School of Civil Engineering, Southeast University, Nanjing, China



# JOURNAL OF MECHANICS OF MATERIALS AND STRUCTURES

[msp.org/jomms](http://msp.org/jomms)

Founded by Charles R. Steele and Marie-Louise Steele

## EDITORIAL BOARD

ADAIR R. AGUIAR	University of São Paulo at São Carlos, Brazil
KATIA BERTOLDI	Harvard University, USA
DAVIDE BIGONI	University of Trento, Italy
MAENGHYO CHO	Seoul National University, Korea
HUILING DUAN	Beijing University
YIBIN FU	Keele University, UK
IWONA JASIUK	University of Illinois at Urbana-Champaign, USA
DENNIS KOCHMANN	ETH Zurich
MITSUTOSHI KURODA	Yamagata University, Japan
CHEE W. LIM	City University of Hong Kong
ZISHUN LIU	Xi'an Jiaotong University, China
THOMAS J. PENCE	Michigan State University, USA
GIANNI ROYER-CARFAGNI	Università degli studi di Parma, Italy
DAVID STEIGMANN	University of California at Berkeley, USA
PAUL STEINMANN	Friedrich-Alexander-Universität Erlangen-Nürnberg, Germany
KENJIRO TERADA	Tohoku University, Japan

## ADVISORY BOARD

J. P. CARTER	University of Sydney, Australia
D. H. HODGES	Georgia Institute of Technology, USA
J. HUTCHINSON	Harvard University, USA
D. PAMPLONA	Universidade Católica do Rio de Janeiro, Brazil
M. B. RUBIN	Technion, Haifa, Israel

**PRODUCTION** [production@msp.org](mailto:production@msp.org)

SILVIO LEVY Scientific Editor

---

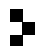
See [msp.org/jomms](http://msp.org/jomms) for submission guidelines.

JoMMS (ISSN 1559-3959) at Mathematical Sciences Publishers, 798 Evans Hall #6840, c/o University of California, Berkeley, CA 94720-3840, is published in 10 issues a year. The subscription price for 2018 is US \$615/year for the electronic version, and \$775/year (+\$60, if shipping outside the US) for print and electronic. Subscriptions, requests for back issues, and changes of address should be sent to MSP.

---

JoMMS peer-review and production is managed by EditFLOW<sup>®</sup> from Mathematical Sciences Publishers.

PUBLISHED BY

 **mathematical sciences publishers**  
nonprofit scientific publishing

<http://msp.org/>

© 2018 Mathematical Sciences Publishers

# Journal of Mechanics of Materials and Structures

Volume 13, No. 3

May 2018

- 
- Formulas for the H/V ratio of Rayleigh waves in compressible prestressed hyperelastic half-spaces** PHAM CHI VINH, THANH TUAN TRAN, VU THI NGOC ANH and LE THI HUE 247
- Geometrical nonlinear dynamic analysis of tensegrity systems via the corotational formulation** XIAODONG FENG 263
- Shaft-hub press fit subjected to couples and radial forces: analytical evaluation of the shaft-hub detachment loading** ENRICO BERTOCCHI, LUCA LANZONI, SARA MANTOVANI, ENRICO RADI and ANTONIO STROZZI 283
- Approximate analysis of surface wave-structure interaction** NIHAL EGE, BARIŞ ERBAŞ, JULIUS KAPLUNOV and PETER WOOTTON 297
- Tuning stress concentrations through embedded functionally graded shells** XIAOBAO LI, YIWEI HUA, CHENYI ZHENG and CHANGWEN MI 311
- Circular-hole stress concentration analysis on glass-fiber-cotton reinforced MC-nylon** YOU RUI TAO, NING RUI LI and XU HAN 337
- Elastic moduli of boron nitride nanotubes based on finite element method** HOSSEIN HEMMATIAN, MOHAMMAD REZA ZAMANI and JAFAR ESKANDARI JAM 351
- Effect of interconnect linewidth on the evolution of intragranular microcracks due to surface diffusion in a gradient stress field and an electric field** LINYONG ZHOU, PEIZHEN HUANG and QIANG CHENG 365
- Uncertainty quantification and sensitivity analysis of material parameters in crystal plasticity finite element models** MIKHAIL KHADYKO, JACOB STURDY, STEPHANE DUMOULIN, LEIF RUNE HELLEVIK and ODD STURE HOPPERSTAD 379
- Interaction of shear cracks in microstructured materials modeled by couple-stress elasticity** PANOS A. GOURGIOTIS 401



1559-3959(2018)13:3;1-Z